ROYAL SOCIETY OF CHEMISTRY

EDGE ARTICLE

Check for updates

All publication charges for this article have been paid for by the Royal Society of Chemistry

Acene enlargement for absorption red-shifting and photosensitization enhancement of photosensitizers with aggregation-induced emission†

Qiang Wang,[a] Chunbin Li,[b] Yuchen Song,[a] Qiankun Shi,[a] Heng Li,[c] Hua Zhong,*[c] Jianguo Wang*[b] and Fang Hu [ID] *[a]

Photosensitizers with aggregation-induced emission (AIE PSs) were widely explored in photodynamic therapy. Numerous acceptors but few donors were reported to design AIE PSs. In this study, we developed a new kind of donor that can improve the comprehensive performance of AIE PSs by expanding the π extension of aromatic rings at the end of the triphenylamine group through acene enlargement. The absorption and fluorescence peaks of anthryl-substituted AIE PS are red-shifted by 29 nm and 42 nm; the photosensitization efficiency is enhanced by 1.16 times; the AIE factor is 86.1 and the fluorescence quantum yield is 9.3%. We also demonstrated that the anthryl-based AIE PS can image and ablate cancer cells well both *in vitro* and *in vivo*. The anthryl-triphenylamine donor provides an excellent option to design donor–acceptor AIE PSs with high comprehensive performance.

Introduction

Photodynamic therapy (PDT) has attracted extensive attention in cancer treatment on account of its noninvasive treatment and spatiotemporal selectivity. It involves the use of light-excited photosensitizers (PSs) to transfer energy to the surrounding molecular oxygen, generating therapeutic reactive oxygen species (ROS).[1–3] As the key factors in PDT, various PSs have been designed so far. For example, several porphyrin- and chlorin-based PSs are successful in clinical practice.[4–6] But the PDT efficiency of these PSs is limited due to the hydrophobic and planar structures, which promote the formation of aggregates in aqueous media. In the aggregates, the strong π–π stacking consumes the excited state of the PSs through non-radiative decay pathways, leading to weakened fluorescence emission and decreased ROS production capacity.[7,8] To address this issue, exploring new PSs with aggregation-induced emission (AIE) characteristics is an ingenious solution.[9–12]

Remarkably different from conventional PSs, the twisted structures of AIE PSs can avoid π–π stacking in aggregate state, and the intramolecular motions can be restricted at the same time, resulting in enhanced fluorescence and strong ROS production capacity by reducing the undesired pathways.[13–15]

To improve the photosensitization efficiency of AIE PSs, the promotion of the intersystem crossing (ISC) process from the excited singlet state (S_n) to the triplet state (T_n) is required. Most AIE PSs have a donor–acceptor (D–A) structure, which can reduce the singlet–triplet energy gap and benefit the ISC process. To further improve the efficiency of the AIE PSs with a D–A structure, three main methods are generally used to further promote the ISC process.[16–18] The first method is increasing the dihedral angle between the donor and acceptor units by increasing the steric hindrance or conjugation length, which can separate the highest energy occupied molecular orbital (HOMO) and the lowest energy unoccupied molecular orbital (LUMO) distribution and reduce the energy gap between S_n and T_n.[19,20] By reducing this energy gap, AIE PSs with expected ISC efficiency are obtained. However, the steric hindrance or conjugated linker would weaken the intramolecular charge transfer (ICT) between the donor and acceptor and make the absorption peak blue-shifted, which is disadvantageous for PDT. The second method is tuning the number of the donor unit and acceptor unit in AIE PSs. It is reported that the reduced energy gap between S_n and T_n can be obtained when more acceptor units than donor units are contained in the molecular structure.[21] The third method is extending the conjugation polymerization of AIE PSs. With increased conjugation

[a] Guangdong Provincial Key Laboratory of Construction and Detection in Tissue Engineering, Biomaterials Research Center, School of Biomedical Engineering, Southern Medical University, Guangzhou 510515, China. E-mail: hufang19@smu.edu.cn

[b] College of Chemistry and Chemical Engineering, Inner Mongolia Key Laboratory of Fine Organic Synthesis, Inner Mongolia University, Hohhot 010021, China. E-mail: wangjg@imu.edu.cn

[c] Department of Orthopaedics, The Fifth Affiliated Hospital, Southern Medical University, Guangzhou 510900, China. E-mail: zhong8099@163.com

† Electronic supplementary information (ESI) available. See DOI: https://doi.org/10.1039/d2sc05454j

polymerization, the energy of the upper excited states decreases and goes closer to the lowest excited states, giving more channels for the ISC process to facilitate ROS production.[22,23] However, the latter two methods contribute little to the absorption red-shifting, which is beneficial for light penetration and highly desired for the development of AIE PSs.

Selecting proper acceptor or donor units, especially the strong electron-withdrawing units, to enhance the ICT is an effective way to obtain AIE PSs with red-shifted absorption. For example, the tetracyanoanthra-*p*-quinodimethane or (3-cyano-5*H*-furan-2-ylidene)malononitrile unit can make the absorption peak of AIE PSs located in the green area.[24,25] The malononitrile-modified indane, 2-(9*H*-fluoren-9-ylidene)malononitrile or diketopyrrolopyrrole units can even red-shift the absorption peaks of AIE PSs to the red area.[26–28] Numerous acceptors are reported with good performance. Unlike the acceptor units, there are few alternatives for the donor units. Mostly, triphenylamine or tetraphenylethylene serves as the donor unit. Sometimes the electron-donating alkoxy is modified on the end of triphenylamine or tetraphenylethylene to red-shift the absorption. However, the electron-donating alkoxy may harm the fluorescence efficiency and even the ROS production capacity.[29] It would be advantageous if the donor unit that can improve the comprehensive performance including red-shifted absorption, high fluorescence efficiency, and ROS production capacity is available.

In this study, we developed new donor units for AIE PS construction by enlarging the π extension at the end of triphenylamine group and realized red-shifted absorption, enhanced photosensitization, and preserved fluorescence intensity at the same time. As generally used donor unit for AIE molecules, triphenylamine can contribute more than tetraphenylethylene to the red-shifting of absorption peak. Triphenylamine together with electron-withdrawing fumaronitrile can form an AIE PS with a D–A structure (TFN, Scheme 1). It is found that the absorption of TFN is red-shifted after modifying the end of triphenylamine units with methoxyl groups (MeO-TFN), but the photosensitization and fluorescence efficiencies are reduced. By replacing the electron-donating methoxyl with π-extension acenes, the absorption peaks are gradually red-

shifted and the photosensitization efficiencies are enhanced from phenyl to naphthyl (Nap-TFN), then to anthryl substitutions (Ant-TFN). Meanwhile, the fluorescence quantum yields (Φ_F) of the acene-substituted AIE PS remain high compared to the methoxyl-substituted one, and the AIE factors ($\alpha_{AIE} = \Phi_{F,aggregate}/\Phi_{F,solution}$) of the anthryl-substituted AIE PS increase much. We also demonstrate that the anthryl-substituted AIE PS owns the best photosensitization performance, and it can ablate cancer cells effectively *via* PDT both *in vitro* and *in vivo*. This study, thus, introduces a new acene-substituted triphenylamine capable of improving the comprehensive performances of AIE PS when serving as donor units.

Results and discussion

Red-shifted absorption and preserved fluorescence of acene-substituted AIE PS

The synthetic routes of the designed molecules are shown in Scheme S1.† TFN, MeO-TFN, and Nap-TFN were synthesized *via* a one-step Buchwald–Hartwig cross-coupling reaction. Ant-TFN was synthesized *via* two-step Buchwald–Hartwig cross-coupling reactions. It was started from the reaction between 2-bromoanthracene and aniline to yield intermediates *N*-phenylanthracen-2-amine, then coupled with bis(4-bromophenyl)fumaronitrile to yield Ant-TFN. The chemical structures were well characterized by ^{1}H NMR, ^{13}C NMR, and mass spectrometry.
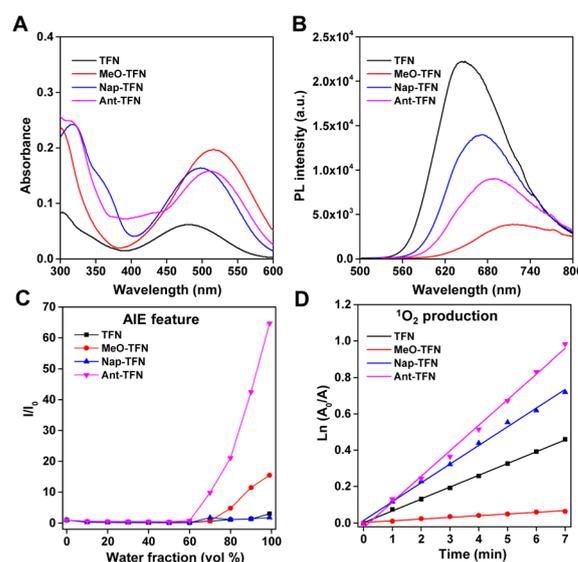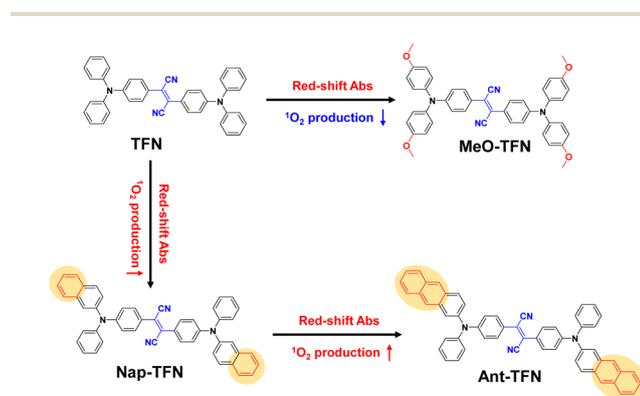

Fig. 1 Optical properties. Absorption (A) and fluorescence (B) spectra of TFN, MeO-TFN, Nap-TFN and Ant-TFN (10 µM) in DMSO/water (1/99, v/v). (λ_{ex} = 482 nm for TFN, λ_{ex} = 514 nm for MeO-TFN, λ_{ex} = 497 nm for Nap-TFN, λ_{ex} = 511 nm for Ant-TFN). (C) Relative fluorescence intensities of TFN, MeO-TFN, Nap-TFN, and Ant-TFN with different water fractions at the maximum emission wavelength. (D) Decomposition rates of ABDA in the presence of TFN, MeO-TFN, Nap-TFN, or Ant-TFN under white light irradiation (60 mW cm^{-2}), where A_0 and A are the absorbances of ABDA at 378 nm. [TFN, MeO-TFN, Nap-TFN and Ant-TFN] = 10 µM, [ABDA] = 100 µM.

Scheme 1 The design strategy of Ant-TFN though π-extension acenes to red-shift absorption and improve photosensitization efficiency.

The optical properties of the four compounds were firstly studied. As shown in Fig. 1A and B, the absorption maxima of TFN, MeO-TFN, Nap-TFN, and Ant-TFN aggregates in water are at 482 nm, 514 nm, 497 nm, and 511 nm, respectively, and the fluorescence maxima are at 646 nm, 710 nm, 667 nm, and 688 nm, respectively. After modifying TFN with four electron-donating methoxyl groups, the ICT is obviously enhanced and the absorption maximum of MeO-TFN is red-shifted by 32 nm. Similar to the ICT enhancing method, the π extension method can also red-shift the absorption maximum. By replacing the phenyl on the end of triphenylamine units with naphthyl or anthryl, the absorption maxima of Nap-TFN and Ant-TFN are red-shifted by 15 nm and 29 nm, respectively. By expanding the π extension, the molar absorption coefficient of Nap-TFN and Ant-TFN is increased to 2.6 times and 2.5 times of TFN, respectively. It is beneficial to increase ROS production capacity by enhancing the light harvesting capability. The fluorescence maxima of MeO-TFN, Nap-TFN, and Ant-TFN are also relevantly red-shifted compared to TFN upon ICT improvement or π extension. By referring to 4-(dicyanomethylene)-2-methyl-6-(4-dimethylaminostyryl)-4H-pyran (DCM), the Φ_F of TFN, MeO-TFN, Nap-TFN, and Ant-TFN aggregates in water were measured to be 15.1%, 2.7%, 9.9%, and 9.3%, respectively (Fig. S1†). These results indicate that the enhanced ICT and π extension can both red-shift the absorption and fluorescence wavelength, however, the enhanced ICT in this system severely reduces the fluorescence efficiency of D–A luminophores while the π extension does not damage the efficiency too much.

The π extension can increase the molecular planarity, which has a risk to damage the AIE feature. Therefore, the AIE features of TFN, MeO-TFN, Nap-TFN, and Ant-TFN were determined by measuring their fluorescence intensities in the THF/water solutions with different water fractions. As shown in Fig. S2,† TFN, MeO-TFN, Nap-TFN, and Ant-TFN have weak fluorescence in the THF solution. Along with the increment of water factions from 0 to 60%, their fluorescence intensities gradually increase. When the water fractions increase from 60% to 99%, their fluorescence intensities are enhanced, exhibiting obvious AIE features (Fig. 1C). By comparing the Φ_F of the aggregates in water with the solutions in THF, the α_{AIE} of TFN, MeO-TFN, Nap-TFN, and Ant-TFN were calculated to be 4.8, 18.4, 1.83, and 86.1, respectively. By extending the π conjugation, the α_{AIE} of Nap-TFN becomes lower than TFN. Oppositely, the α_{AIE} of Ant-TFN becomes 18 times of TFN after further π extension, indicating that the anthryl substitution can greatly improve the AIE feature of TFN. This is perhaps due to the reduction of integral planarity of the molecules by the large steric hindrance of anthryl groups, though the local planarity is increased.

Enhanced photosensitization of acene-substituted AIE PS

The photosensitization efficiency was then estimated by using 9,10-anthryl-bis(methylene)dimalonic acid (ABDA) as a probe to detect the singlet oxygen ($^1O_2$) production capacity. As shown in Fig. S3,† TFN, MeO-TFN, Nap-TFN and Ant-TFN can all gradually decompose ABDA (100 μM) within 7 min upon light irradiation, indicating $^1O_2$ production ability. Since the reaction

between $^1O_2$ and ABDA is a first-order reaction, the comparison of the $^1O_2$ production capacities is exhibited by calculating the slopes of the straight lines from $\ln(A_0/A)$ *vs.* irradiation time plots (Fig. 1D).[30] As summarized in Table 1, with increased ICT, the $^1O_2$ production capacity of MeO-TFN decreases to 14% of TFN; with increased π extension, the $^1O_2$ production capacity of Nap-TFN increases to 1.58 times of TFN, while that of Ant-TFN increases to 2.16 times. The ROS production capacities are also measured by using DCFH as a fluorescent probe, which indicates the same rank: Ant-TFN > Nap-TFN > TFN > MeO-TFN (Fig. S4†). Meanwhile, the Nap-TFN and Ant-TFN have larger ROS production capacities than Ce6, a Food and Drug Administration-approved photosensitizer. Since anthracene can be oxidized by $^1O_2$ to generate endoperoxide, it is concerned that Ant-TFN is not stable during the photosensitization process. The mass spectrum indicates that the endoperoxides do generate upon irradiation of Ant-TFN (Fig. S5 and S6†). Fortunately, the NMR spectrum indicates that only around 10% Ant-TFN was oxidized upon light irradiation (350 mW cm^{-2}, 12 min, Fig. S7†). The ROS production capacity of Ant-TFN after oxidation remained 91%, which is still 1.97 times of TFN (Fig. S8†).

Overall, the ICT increment by introducing electron-donating methoxyl groups can only red-shift the absorption and fluorescence wavelength but severely decrease the fluorescence and $^1O_2$ production efficiencies of AIE PSs; the π extension through acene enlargement can not only red-shift the absorption and fluorescence wavelength but also increase the $^1O_2$ production efficiency without damaging the fluorescence efficiency too much. Meanwhile, the anthryl groups can greatly increase the α_{AIE} at the same time.

The mechanism for red-shifted absorption and enhanced photosensitization

To figure out the mechanism of the red-shifted absorption and enhanced $^1O_2$ production capacity through acene enlargement, the optimized molecular structures were obtained by Gaussian software. The HOMO and LUMO distributions and orbitals are shown in Fig. 2A. Compared to TFN, the energy gaps between HOMO and LUMO orbitals of MeO-TFN, Nap-TFN, and Ant-TFN are all reduced, which can result in red-shifted absorptions. Detailly, the narrowed HOMO–LUMO gap in MeO-TFN is mainly caused by the increased energy levels of HOMO due to the electron-donating effect of methoxyl groups; in Nap-TFN and

Table 1 The summary of the optical properties

AIE PS	λ_{ex} (nm)	λ_{em} (nm)	$\Phi_F{}^a$ (%)	$\alpha_{AIE}{}^b$	$^1O_2$ production^c
TFN	482	646	15.1	4.8	1
MeO-TFN	514	710	2.7	18.4	0.14
Nap-TFN	497	667	9.9	1.83	1.58
Ant-TFN	511	688	9.3	86.1	2.16

^{a} Relative fluorescence quantum yields were measured by referring to DCM. Φ_F(DCM) = 43.5%. ^{b} $\alpha_{AIE} = \Phi_{F, aggregate}/\Phi_{F, solution}$. ^{c} Relative $^1O_2$ production capacities by referencing TFN aggregates.
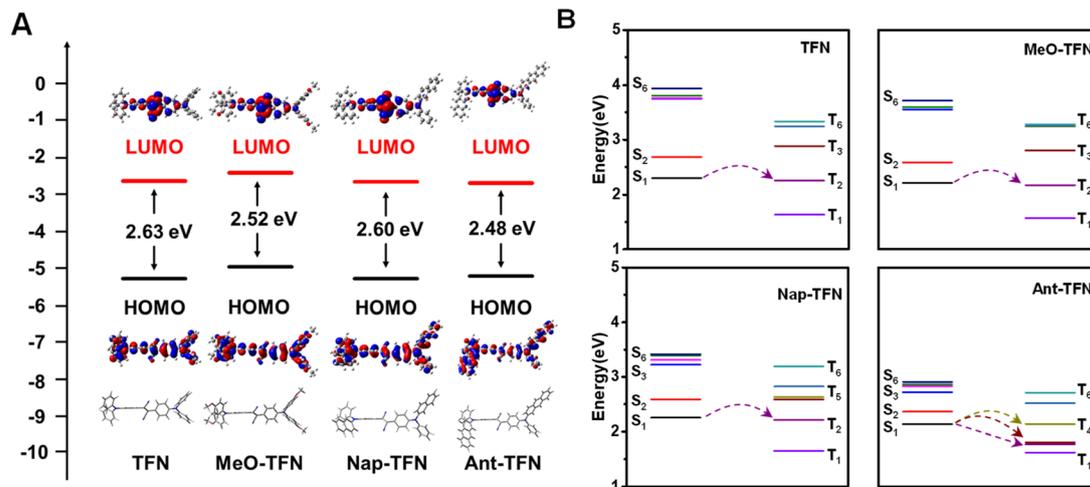
Fig. 2 TD-DFT calculations. (A) HOMO–LUMO distributions, energy gaps, and optimized structures of TFN, MeO-TFN, calculated by DFT (Gaussian 09/B3LYP/6-311g(d)). (B) Singlet and triplet excited states of TFN, MeO-TFN, Nap-TFN, and Ant-TFN calculated by TD-DFT, the arrows indicate the energy gap between S_1 and T_n smaller than 0.3 eV to benefit ISC channels.

Ant-TFN, the narrowed HOMO–LUMO gaps are caused by the increased energy levels of HOMO and the decreased energy levels of LUMO, which are ascribed to the electron delocalization, especially the HOMO distributions, to the extended π conjugation. The time-dependent density functional theory (TD-DFT) calculations were then investigated to evaluate the singlet and triplet excited states of TFN, MeO-TFN, Nap-TFN, and Ant-TFN, respectively. The S_n and T_n ($n = 1$–6) orbital levels of the four AIE PSs are shown in Fig. 2B. MeO-TFN has similar S_n and T_n ($n = 1$–6) orbital distributions to TFN, therefore, no ISC promotion occurs in MeO-TFN. For Nap-TFN and Ant-TFN, the higher excited states (S_n and T_n, $n = 2$–6) go closer to the first excited states (S_1 and T_1) and the distributions become denser with increased π extension, which can promote the ISC process for $^1O_2$ production. In addition, the singlet–triplet ISC process is more beneficial when the energy gap between S_1 and T_n is smaller than 0.3 eV. According to the TD-DFT calculations, only the channel from S_1 to T_2 is beneficial in TFN, MeO-TFN, and Nap-TFN, while multiple channels from S_1 to T_2, T_3, and T_4 are beneficial in Ant-TFN. Therefore, the increased number of beneficial singlet-triplet transition channels should also be the reason that the ROS production capacity of Ant-TFN is highly enhanced.

We further explored the generalizability of the acene enlargement method by using 2-(diphenylmethylene)malononitrile as a new acceptor. The new PSs (TMN, Nap-TMN, and Ant-TMN) were synthesized and characterized by ^{1}H NMR, and ^{13}C NMR (Fig. S25–S30†). The absorption and fluorescence properties (Fig. S9†) and ROS production capacities (Fig. S10) are summarized in Table S1.† The comprehensive performances of these PSs, including absorption, fluorescence and ROS production capacity, are improved in the same way of the ones with 2,3-diphenylfumaronitrile as acceptor. These results indicate that acene enlargement of triphenylamine is still a valid method to improve the performances of AIE PSs when the donor changed.

Photodynamic ablation of cancer cells *in vitro*

To evaluate the intracellular performance, the four AIE PSs are prepared into water dispersive nanoparticles (NPs) by using DSPE-PEG$_{2000}$ as the polymer matrix (Fig. 3A). The average sizes of TFN NPs, MeO-TFN NPs, Nap-TFN NPs, and Ant-TFN NPs are all around 80 nm as measured by dynamic light scattering (DLS) and transmission electron microscopy (Fig. S11†). In addition, the DLS sizes of the four PS NPs are hardly changed within 7 days, indicating good stability (Fig. S12†). The absorption maxima of TFN NPs, MeO-TFN NPs, Nap-TFN NPs, and Ant-TFN NPs are at 483 nm, 509 nm, 492 nm, and 509 nm, respectively; the fluorescence maxima are at 642 nm, 714 nm, 665 nm, and 690 nm, respectively (Fig. 3B); and the $^1O_2$ production capacity
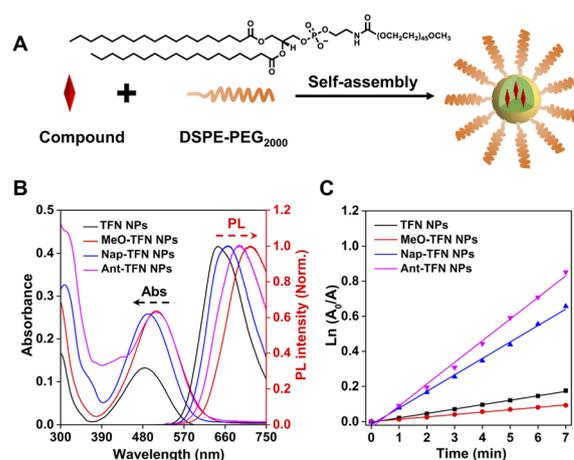

Fig. 3 Optical properties of NPs. (A) The schematic synthesis of PS NPs. Absorption and fluorescence spectra (B), and $^1O_2$ production capacities (C) of TFN NPs, MeO-TFN NPs, Nap-TFN NPs, and Ant-TFN NPs (10 μM) in water. ($\lambda_{ex} = 483$ nm for TFN NPs, $\lambda_{ex} = 492$ nm for Nap-TFN NPs, $\lambda_{ex} = 509$ nm for MeO-TFN and Ant-TFN NPs). The light power intensity is 60 mW cm^{-2}.

is MeO-TFN NPs < TFN NPs < Nap-TFN NPs < Ant-TFN NPs (Fig. 3C and S13†). The ROS production capacities of the NPs are also measured by using DCFH as a fluorescent probe, which indicate the same trends (Fig. S14†). All these optical properties of the NPs remain similar to the aggregates in water.

Live cell imaging of AIE PS NPs was evaluated against 4T1 cells by confocal laser scanning microscopy (CLSM). As shown in Fig. S15,† 4T1 cells treated with AIE NPs exhibit gradually increased red fluorescence in the cytoplasm with the prolonged incubation time, which reaches a peak at 8 h. TFN NPs have very bright fluorescence signals in 4T1 cells. Though the signals of Nap-TFN and Ant-TFN NPs are weaker than TFN NPs, the fluorescence signals can obviously be seen after 1 h incubation. The signals of MeO-TFN are much weaker than the others due to the low fluorescence quantum yield. The red-shifted absorption wavelength and preserved fluorescence efficiency enable Ant-TFN a good agent for cell imaging.

Subsequently, the intracellular ROS production and cancer cell ablation capacities of the AIE PS NPs were assessed. Non-fluorescent DCFH-DA is selected as a probe to identify the intracellular ROS production (Fig. 4A), which can react with ROS to produce green-fluorescent 2′,7′-dichlorofluorescein (DCF). Upon light irradiation, almost no green fluorescence was observed in TFN and MeO-TFN NPs treated 4T1 cells due to low $^1O_2$ production capability (Fig. 4B). In the same conditions, Nap-TFN and Ant-TFN NPs could both generate ROS in 4T1 cells, and the latter is stronger than the former, matching well with the $^1O_2$ production capabilities in the water. The live/dead cell staining assay was used to evaluate the 4T1 cell ablation capacities of the AIE PS NPs. As shown in Fig. 4C, the green fluorescence from fluorogenic ester CAM indicates that all four AIE PS NPs have no cytotoxicity in darkness. Upon light irradiation, TFN and MeO-TFN NPs treated 4T1 cells still show green fluorescence, the Nap-TFN NPs treated ones show partly green

and partly red while the Ant-TFN NPs treated ones show mostly red fluorescence from propidium iodide (PI). The results indicate that MeO-TFN NPs and TFN NPs are not competent in cancer cell ablation. After acene enlargement on the end of TFN, the Nap-TFN and Ant-TFN NPs can ablate cancer cells through the PDT process.

The concentration-dependent 4T1 cell PDT efficacy was estimated through MTT assays. As shown in Fig. 5, no obvious cytotoxicity towards 4T1 cells in darkness was observed at 40 µg mL^{-1}, which makes the NPs eligible photosensitizers with low side effects. Upon light irradiation, neither TFN nor MeO-TFN NPs exhibited obvious cytotoxicity towards 4T1 cells because of low $^1O_2$ production capacities even at high concentrations. Both Nap-TFN and Ant-TFN NPs exhibited photo-cytotoxicity towards 4T1 cells. The half-maximal inhibitory concentrations (IC$_{50}$) of Nap-TFN and Ant-TFN NPs are calculated to be 11.23 µg mL^{-1} and 4.36 µg mL^{-1} when the light power intensity is 60 mW cm^{-2} (12 min). The better photodynamic therapeutic efficiency of Ant-TFN NPs matches well with the higher $^1O_2$ production capacity.

Imaging and PDT of cancer cells *in vivo*

We further verified the performance of Ant-TFN NPs *in vivo* by using 4T1 tumor-bearing BALB/c mice. Firstly, the hemolytic activity of Ant-TFN NPs was checked. Ant-TFN NPs caused no hemolysis even at the high concentration of 100 µg mL^{-1} (Fig. S16†). As shown in Fig. 6A and S17,† with intravenously injected Ant-TFN NPs, a fluorescence accumulation was persistently observed at the tumor site and reached a plateau after 24 h, which suggests effective accumulation of nanoparticles into the tumor region attributed to the enhanced
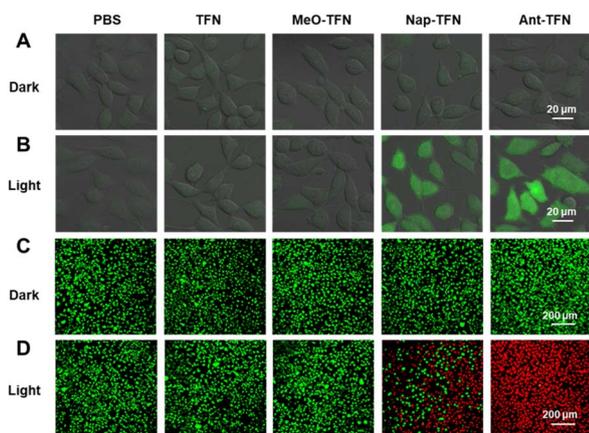

Fig. 4 CLSM images of DCFH–DA incubated 4T1 cells after treatment with PBS, TFN NPs, MeO-TFN NPs, Nap-TFN NPs, or Ant-TFN NPs in dark (A) or upon light irradiation (B). CLSM images of 4T1 cells by live/dead cell staining assay after treatment with PBS, TFN NPs, MeO-TFN NPs, Nap-TFN NPs or Ant-TFN NPs in dark (C) or upon light irradiation (D). The light power intensity is 60 mW cm^{-2} (12 min). The concentration is 20 µg mL^{-1}.
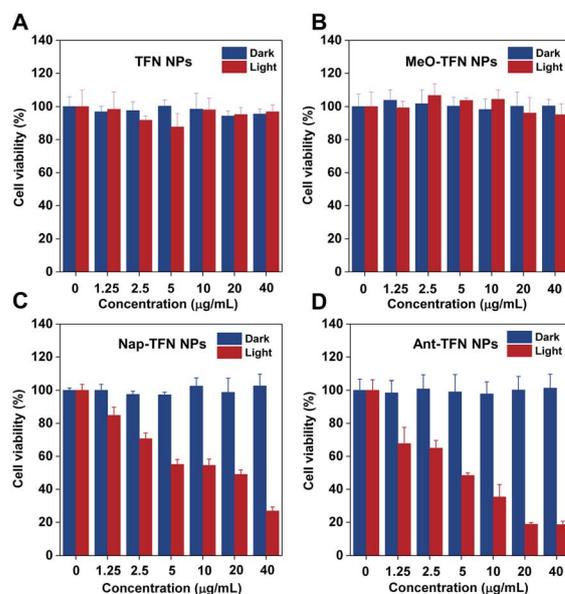

Fig. 5 The 4T1 cell viability upon treatment with different concentrations of TFN NPs (A), MeO-TFN NPs (B), Nap-TFN NPs (C), and Ant-TFN NPs (D) in darkness or upon light irradiation (60 mW cm^{-2}) for 12 min.
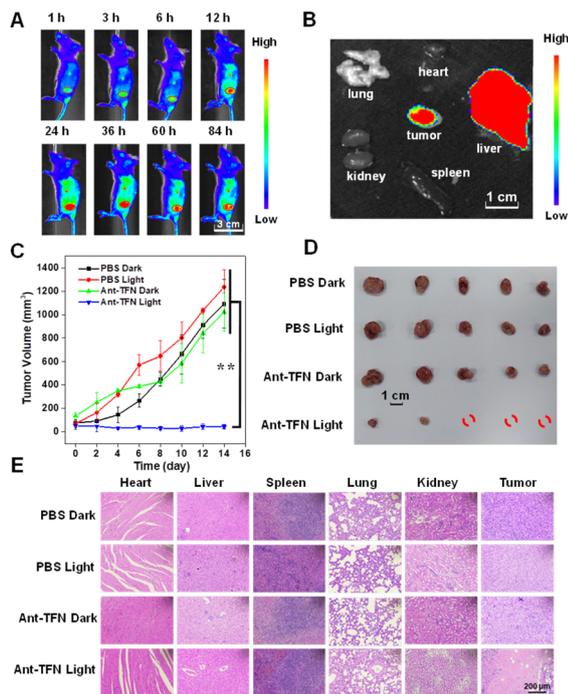
Fig. 6 PDT effect of Ant-TFN NPs *in vivo*. (A) Real-time fluorescence imaging of the mice after intravenous injection with Ant-TFN NPs for 1, 3, 6, 12, 24, 36, 60, and 84 h. (B) The tissue and tumor imaging at 24 h post-injection. (C) The relative tumor volume changes of the mice after treatment with PBS or Ant-TFN NPs with or without the light ($n = 5$, light irradiation during PDT, 300 mW cm^{-2}, 12 min, **$p < 0.01$ determined by Student's t-test). Anatomic mice tumor size (D), and H&E staining (E) of tumor and normal organ tissue sections of different groups of mice after treatment.

permeability and retention effect. After sacrificing mice, the major organs and tumor were collected for *ex vivo* imaging. The fluorescence signals indicate that the injected Ant-TFN NPs mainly distributed in tumor and liver tissues at 24 h post-injection, the PDT treatment timeline (Fig. 6B). As shown in Fig. 6C, the antitumor performance was evaluated by monitoring the tumor growth. The mice were randomly divided into four groups ($n = 5$): (1) PBS, (2) PBS + light, (3) Ant-TFN NPs, (4) Ant-TFN NPs + light; the dosage was 5 mg kg^{-1} by intravenous injection. The tumor volumes were continuously monitored for 14 days. The tumor volumes in the "PBS + light" and "Ant-TFN NPs" groups rose as fast as in the PBS control group. In the "Ant-TFN NPs + light" group, the tumor growth could be inhibited; some tumors were even cleared. After 14 days, the planted tumors were taken out through resection to compare the sizes and weights directly. The tumor sizes in this "Ant-TFN NPs + light" group were obviously smaller than in other groups (Fig. 6D), indicating that Ant-TFN NPs can undergo effect PDT *in vivo*. The therapeutic effect and safety of the Ant-TFN NPs were further estimated by H&E staining and body weight. As illustrated in Fig. 6E, the tumor tissue was damaged in the "Ant-TFN NPs + light" group but kept intact in other groups. Meanwhile, no obvious abnormal morphologies were observed in the main normal tissues including the heart, liver, spleen, lung, and

kidney in the four groups. The H&E staining indicates that Ant-TFN NPs would not damage the organs when destroying the tumor through PDT process. The body weights of the mice were monitored every 2 days during the treatment, and all grew stably (Fig. S18†). In addition, the blood routine examinations also exhibit the good biocompatibility of Ant-TFN NPs (Table S2†). Taking the results of mice without tumors as a reference, red blood cells and the blood platelet systems in all groups were mostly in the normal range.

Conclusions

In summary, we have successfully developed an advantageous donor for D-A AIE PS to improve the comprehensive performances by enlarging the acenes on the end of triphenylamine. After substitution of the phenyls by π-extended naphthyl or anthryl, the absorption peak of generated Nap-TFN or Ant-TFN was red-shifted by 15 nm or 29 nm. Though the electron-donating methoxyl substituted TFN (MeO-TFN) can also red-shift the absorption peak, the fluorescence efficiency and photosensitization efficiency are dramatically decreased compared to TFN. For the π-extended Nap-TFN and Ant-TFN, their $^1O_2$ production efficiencies increase to 1.58 times and 2.16 times of TFN, and their Φ_F are as high as 9.9% and 9.3%. Meanwhile, the α_{AIE} of Ant-TFN was estimated to be 86.1, extremely larger than TFN. With high comprehensive performances, the Ant-TFN NPs can not only image but also inhibit 4T1 cells both *in vitro* and *in vivo*. The newly developed donor provides an excellent alternative for designing D–A AIE PS with red-shifted absorption, preserved fluorescence efficiency, and enhanced photosensitization.

Data availability

All the data supporting this article have been included in the main text and the ESI.†

Author contributions

F. H., J. W. and H. Z. contribute to the conceptualization and supervision. Q. W., Y. S., Q. S. and H. L. contribute to the methodology. Q. W. and C. L. contribute to the software. Q. W. and F. H. contribute to the original draft writing. Q. W., F. H. J. W. and H. Z. contribute to the review & editing.

Conflicts of interest

There are no conflicts to declare.

Acknowledgements

References

1 D. W. Felsher, *Nat. Rev. Cancer*, 2003, **3**, 375.

2 A. P. Castano, P. Mroz and M. R. Hamblin, *Nat. Rev. Cancer*, 2006, **6**, 535.

3 P. Agostinis, K. Berg, K. A. Cengel, T. H. Foster, A. W. Girotti, S. O. Gollnick, S. M. Hahn, M. R. Hamblin, A. Juzeniene, D. Kessel, M. Korbelik, J. Moan, P. Mroz, D. Nowis, J. Piette, B. C. Wilson and J. Golab, *Ca-Cancer J. Clin.*, 2011, **61**, 250.

4 X. Li, J. F. Lovell, J. Yoon and X. Chen, *Nat. Rev. Clin. Oncol.*, 2020, **17**, 657.

5 D. van Straten, V. Mashayekhi, H. S. de Bruijn, S. Oliveira and D. J. Robinson, *Cancers*, 2017, **9**, 19.

6 G. B. Kharkwal, S. K. Sharma, Y. Y. Huang, T. Dai and M. R. Hamblin, *Lasers Surg. Med.*, 2011, **43**, 755.

7 K. Liu, Y. Liu, Y. Yao, H. Yuan, S. Wang, Z. Wang and X. Zhang, *Angew. Chem., Int. Ed.*, 2013, **52**, 8285.

8 Q. Zang, J. Yu, W. Yu, J. Qian, R. Hu and B. Z. Tang, *Chem. Sci.*, 2018, **9**, 5165.

9 X. Cai and B. Liu, *Angew. Chem., Int. Ed.*, 2020, **59**, 9868.

10 S. Liu, G. Feng, B. Z. Tang and B. Liu, *Chem. Sci.*, 2021, **12**, 6488.

11 Q. Wan, R. Zhang, Z. Zhuang, Y. Li, Y. Huang, Z. Wang, W. Zhang, J. Hou and B. Z. Tang, *Adv. Funct. Mater.*, 2020, **30**, 2002057.

12 G. Feng and B. Liu, *Acc. Chem. Res.*, 2018, **51**, 1404.

13 Y. Gao, X. Wang, X. He, Z. He, X. Yang, S. Tian, F. Meng, D. Ding, L. Luo and B. Z. Tang, *Adv. Funct. Mater.*, 2019, **29**, 1902673.

14 G. Yuan, C. Lv, J. Liang, X. Zhong, Y. Li, J. He, A. Zhao, L. Li, Y. Shao, X. Zhang, S. Wang, Y. Cheng and H. He, *Adv. Funct. Mater.*, 2021, **31**, 2104026.

15 G. Yang, J. S. Ni, Y. Li, M. Zha, Y. Tu and K. Li, *Angew. Chem., Int. Ed.*, 2021, **60**, 5386.

16 F. Hu, S. Xu and B. Liu, *Adv. Mater.*, 2018, **30**, 1801350.

17 E. M. Stennett, M. A. Ciuba and M. Levitus, *Chem. Soc. Rev.*, 2014, **43**, 1057.

18 S. Xu, W. Wu, X. Cai, C. J. Zhang, Y. Yuan, J. Liang, G. Feng, P. Manghnani and B. Liu, *Chem. Commun.*, 2017, **53**, 8727.

19 S. Xu, Y. Yuan, X. Cai, C. J. Zhang, F. Hu, J. Liang, G. Zhang, D. Zhang and B. Liu, *Chem. Sci.*, 2015, **6**, 5824.

20 S. Gao, S. Yu, Y. Zhang, A. Wu, S. Zhang, G. Wei, H. Wang, Z. Xiao and W. Lu, *Adv. Funct. Mater.*, 2021, **31**.

21 S. Liu, H. Zhang, Y. Li, J. Liu, L. Du, M. Chen, R. T. K. Kwok, J. W. Y. Lam, D. L. Phillips and B. Z. Tang, *Angew. Chem., Int. Ed.*, 2018, **57**, 15189.

22 T. Zhou, R. Hu, L. Wang, Y. Qiu, G. Zhang, Q. Deng, H. Zhang, P. Yin, B. Situ, C. Zhan, A. Qin and B. Z. Tang, *Angew. Chem., Int. Ed.*, 2020, **59**, 9952.

23 W. Wu, D. Mao, S. Xu, Kenry, F. Hu, X. Li, D. Kong and B. Liu, *Chem*, 2018, **4**, 1937.

24 W. Wu, D. Mao, F. Hu, S. Xu, C. Chen, C. J. Zhang, X. Cheng, Y. Yuan, D. Ding, D. Kong and B. Liu, *Adv. Mater.*, 2017, **29**, 1700548.

25 W. Wu, D. Mao, S. Xu, M. Panahandeh-Fard, Y. Duan, F. Hu, D. Kong and B. Liu, *Adv. Funct. Mater.*, 2019, **29**, 1901791.

26 D. Wang, M. M. S. Lee, W. Xu, G. Shan, X. Zheng, R. T. K. Kwok, J. W. Y. Lam, X. Hu and B. Z. Tang, *Angew. Chem., Int. Ed.*, 2019, **58**, 5628.

27 J. Zou, Z. Yin, P. Wang, D. Chen, J. Shao, Q. Zhang, L. Sun, W. Huang and X. Dong, *Chem. Sci.*, 2018, **9**, 2188.

28 L. Feng, C. Li, L. Liu, Z. Wang, Z. Chen, J. Yu, W. Ji, G. Jiang, P. Zhang, J. Wang and B. Z. Tang, *ACS Nano*, 2022, **16**, 4162.

29 D. Wang, H. Su, R. T. K. Kwok, G. Shan, A. C. S. Leung, M. M. S. Lee, H. H. Y. Sung, I. D. Williams, J. W. Y. Lam and B. Z. Tang, *Adv. Funct. Mater.*, 2017, **27**, 1704039.

30 N. A. Kuznetsova, N. S. Gretsova, O. A. Yuzhakova, V. M. Negrimovskii, O. L. Kaliya and E. A. Luk'yanets, *Russ. J. Gen. Chem.*, 2001, **71**, 36.